IEEE Access
Multidisciplinary | Rapid Review | Open Access Journal

Received August 16, 2019, accepted August 22, 2019, date of publication August 30, 2019, date of current version September 13, 2019.

Digital Object Identifier 10.1109/ACCESS.2019.2938615

A Novel Transformation Optics-Based FDTD Algorithm for Fast Electromagnetic Analysis of Small Structures in a Large Scope

RUONAN CHEN[1], LEI KUANG[1], (Member, IEEE), ZHENGQI ZHENG[1], AND QING HUO LIU[2], (Fellow, IEEE)

[1]Shanghai Key Laboratory of Multidimensional Information Processing, Engineering Center of SHMEC for Space Information and GNSS, School of Information Science and Technology, East China Normal University, Shanghai 200241, China
[2]Department of Electrical and Computer Engineering, Duke University, Durham, NC 27708, USA

Corresponding author: Lei Kuang (lkuang@ee.ecnu.edu.cn)

This work was supported in part by the National Natural Science Foundation of China under Grant 61571190, Grant 61871184, and Grant 61771197.

ABSTRACT In this paper, we present a novel Transformation Optics based Finite-difference time-domain (TO-FDTD) algorithm with Square Transformed Region, which is suitable for fast electromagnetic analysis of small structures in a large computational domain. A small structure can be solved with coarse grids in a transformed region, since it is enlarged by transformation optics. No fine grid is applied for the small structure so that computational efficiency can be improved greatly. In addition, the TO-FDTD algorithm can also avoid time-space field interpolations and the late-time instability of the subgridding algorithm. To eliminate the staircasing errors introduced by curved boundaries of its transformed region, we propose the square transformed region instead of the circular one. We parameterize the square boundary in polar coordinates so that it is easy to be implemented. Through coordinate transformation, new anisotropic permittivity and permeability can be obtained in the transformed region. Then we develop a stable anisotropic FDTD algorithm to solve the transformed Maxwell's Equations. Numerical results on diffraction and scattering of small structures show that our proposed TO-FDTD algorithm has high computational efficiency and accuracy.

INDEX TERMS Finite-difference time-domain (FDTD), staircasing errors, transformation optics.

I. INTRODUCTION

The finite-difference time-domain (FDTD) scheme [1] has been well established for various electromagnetic simulations. It has a number of advantages such as its simplicity, ability to easily model complex geometric problem, and ability to handle dispersive materials. The geometrical optics is suitable to simulate electrically large objects instead of electrically small objects [2]. The transmission Line Theory is suited for the reflection and transmission coefficients of a multi-layer structure, but not for scattering of the complex object [3]. In contrast, the FDTD algorithm is suitable to simulate objects with arbitrary shapes and electrically small objects. Compared with the Dyadic Green's Function, which is combined with numerical methods (e.g. Method of Moment) to solve integral equations for complex targets [4], the FDTD algorithm has its merits in being simple and free of a system matrix solution (matrix-free), ability to easily model complex geometric, inhomogeneous and dispersive problem. However, one of the major limitations of the FDTD algorithm is huge computational burden of simulating small structures in a large computational domain, i.e., the coexistence of large-scale structures and small-scale structures or small targets in a deep underground site. This is because the spatial grid must be small enough to accurately model small structures. Meanwhile, the maximum time step is limited by the minimum spatial grid size due to the Courant-Friedrich-Levy (CFL) stability condition. Consequently, huge memory requirement and CPU time consumption are required for simulating small structures in a large computational domain.

One popular approach overcoming this problem is the subgridding FDTD algorithm. Fine grids are used to model small structures and coarse grids are used elsewhere. The main difficulty of subgridding technique is the reduced accuracy

The associate editor coordinating the review of this article and approving it for publication was Chan Hwang See.

and late-time instability due to the temporal and spatial interpolations, especially when a grid contrast ratio is large. The large grid contrast ratio with high accuracy was achieved by the Huygens subgridding algorithm [5], [6], but it usually has fairly higher late-time instability. The FDTD subgridding algorithm with separated temporal and spatial subgridding interfaces [7] has higher late-time stability by using two subgridding interfaces for temporal and spatial interpolations separately, but has lower accuracy due to the electric and magnetic field are discontinuous at temporal subgridding interface. Besides, the problem of material traversing subgridding interfaces cannot be solved. To resolve these two problems, a novel FDTD subgridding algorithm with improved separated temporal and spatial interfaces was proposed in [8]. However, there is no universal weighed parameter to interpolate the electric/magnetic fields at the subgridding interfaces. For different simulation scenarios, they need to be determined by different numerical experiments. In order to improve the computational efficiency, the sub-gridded FDTD algorithms with the uniform coarse time step, such as a hybrid sub-gridded scheme [9] and a spatially filtered sub-gridded FDTD scheme [10], have been proposed by Wei et al.. An unsymmetric FDTD subgridding algorithm with unconditional stability proposed in [11] allows for an arbitrary grid contrast ratio. However, the time step need to be found by solving eigenvalues of the matrice. Moreover, the commercial software CST Microwave Studio has been used for electromagnetic analysis [2], [4], [12]. The core algorithm of the CST is Finite Integral Theory (FIT), which has the advantage of simulating electromagnetic phenomena in the time domain, frequency domain and in statics. The subgridding scheme for the FIT [13] can improve the computational efficiency of scattering and diffraction of an electrically small target in a large domain, maintaining the late-time stability. Due to the CFL stability criterion, however, the maximum stable time step in the subgrid is limited by the spatial subgrid size. The smaller time step is needed in the subgrid, thus more CPU time consumption is required.

Recently, transformation optics can be used to design metamaterials to achieve many interesting applications, such as wavelength-sized metastructure [14] capable of solving integral equations, Near-zero-index waveguide [15] that overcomes mode degeneration, attenuation/losses, and energy dispersion of the traditional metallic ones, metamaterial assemblies [16] for optical magnetic field enhancement and chiral plasmonics, curvilinear metasurfaces [17] for surface wave manipulation, graphene acoustic plasmon resonator [18] for ultrasensitive infrared spectroscopy, nanoparticle-based electromagnetic devices [19] for sensing and medical diagnostics, metasurface sensors [20], ENZ-based sensor [21] and surface wave cloaking [22]. Besides, another simple yet useful local mesh refinement algorithm is also based on the transformation optics [23]. Through coordinate transformation, small structures can be enlarged in the transformed region. Therefore, we can simulate the whole computational domain with uniform coarse grids. In comparison to the subgridding algorithm, it eliminates errors by interfaces between coarse and fine grids and avoids the late-time instability problem. However, the transformed region presented in [23] is a circular disk. Due to the inherent drawback of the FDTD algorithm, there are modeling errors between a real curved boundary and its FDTD-modeled boundary. Therefore, staircasing errors are introduced by curved boundaries of the transformed region, using standard Yee grids [1] in regular Cartesian lattices. And staircasing errors increase as the grid size increases. The scattered and diffraction fields from electrically small structures are usually small, so that staircasing errors can lead to larger relative errors. Thus, they cannot be neglected. One way to mitigate staircasing errors is to use a conformal technique. The well-known Contour Path FDTD algorithm (CPFDTD) [24], based on the integral forms of Ampere and Faraday laws, is simple and efficient, but it often leads to late-time instability. A modification of classical CPFDTD algorithm proposed in [25] can eliminate the late-time instability, and maintaining second-order spatial convergence [26]. However, the time step need to be decreased to meet the CFL stability condition, thus will reduce computational efficiency. The Conformal Relaxed Dey-Mittra (CRDM) method [27] enables direct control of the time step reduction, but the time step is still smaller than the standard FDTD time step. A robust conformal FDTD algorithm [28] was proposed to remove the restriction of time step. But it will reduce accuracy due to introducing an artificial magnetic medium in conformal grids. Another algorithm improving the stability proposed in [29] is the Enlarged Cell Technique (ECT). However, the updating equations are more complicated depending on the configuration of the objects.

To eliminate staircasing errors caused by the boundaries of the transformed domain, we present a novel TO-FDTD algorithm in this paper. Instead of using a circular transformed region applied in [23], we enlarge a small region by using a square transformed region. Therefore, no staircasing error is produced near the square boundaries of the transformed region. We parameterize the square boundary in polar coordinates, so that it is easy to be implemented in a simple formulation. By applying Transformation Optics, we obtain new Maxwell's equations with anisotropic permittivity and permeability in the transformed region. Then, according to [30], [31], we develop a stable anisotropic FDTD algorithm for solving electric and magnetic fields in transformed space. The fields in original space can also be obtained by an inverse transformation on corresponding fields in transformed space. We restrict our analysis to two-dimensional (2D) case in this paper. Numerical experiments including scattering and diffraction of small structures have demonstrated accuracy and efficiency of the proposed novel TO-FDTD algorithm.

II. THE TO-FDTD ALGORITHM WITH SQUARE TRANSFORMED REGION

For the TO-FDTD analysis of scattering from a small structure, the staircasing errors introduced by boundaries of a

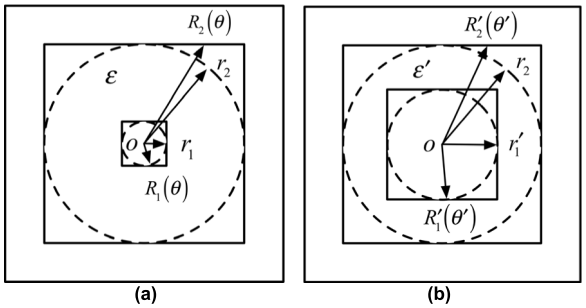

FIGURE 1. Coordinate Transformation. (a) Original space. (b) Transformed space.

circular transformed region cannot be neglected. To avoid these errors, we replace the circular transformed region with the square transformed region, so that the boundaries of the transformed region are aligned with the structured grids. Thus, staircasing errors cannot be introduced by boundaries of the transformed region.

Transformation optics can be interpreted as inhomogeneous and anisotropic compression and stretching of the constituent materials in original space. Based on the invariance of the Maxwell's equations after coordinate transformation, existing FDTD codes can be easily implemented. Acquiring the new anisotropic permittivity and permeability, we develop a stable anisotropic FDTD algorithm for solving Maxwell's equations in the transformed region. Because the small structure is enlarged in the transformed region, uniform coarse grid can be applied globally, and no fine grid needs to be applied for the small structure. Thus, computational efficiency can be improved greatly. Finally, the electromagnetic fields in original space can be obtained by an inverse transformation.

A. TRANSFORMATION OPTICS WITH SQUARE TRANSFORMED REGION

As shown in Figs. 1 (a) and (b), coordinate transformation is applied to a square transformed region, which is divided into a stretched inner square and a compressed outer square annulus.

Boundaries $R_i(\theta)$ of the inner and outer squares in Fig.1 (a) can be parameterized in polar coordinates

$$R_i(\theta) = r_i / \cos\left(\left(\theta - \pi/4\right) \bmod (\pi/2) - \pi/4\right) \quad (i = 1,\ 2) \tag{1}$$

where r_i is the radius of the inscribed dotted circles of the squares, as shown in Fig.1 (a). The indexes 1 and 2 refer to the inner and outer boundaries, respectively. The inner and outer square boundaries $R_i'(\theta')$ in Fig.1 (b) have similar formulations. Note that $\theta = \theta'$ and $R_2(\theta) = R_2'(\theta')$.

Through coordinate transformation, a small square ($r < R_1(\theta)$) in original space is transformed to a large one ($r' < R_1'(\theta')$) in transformed space and the square annulus ($R_1(\theta) < r < R_2(\theta)$) is compressed to a smaller square annulus ($R_1'(\theta') < r < R_2'(\theta')$), by maintaining the outer square boundary $R_2(\theta)$ (or $R_2'(\theta')$) unchanged. A small structure located in the square ($r < R_1(\theta)$) can be stretched to a larger one in the square ($r' < R_1'(\theta')$) by coordinate transformation so that it can be solved with coarse grids. Note that the small structure cannot be enlarged arbitrarily. The trade-off is the square annulus is less resolved due to its smaller area. The arbitrarily enlarged square will result in the arbitrarily compressed square annulus, since the outer boundary of the transformed region is kept unchanged. Although more grids are used to simulate the enlarged square, but less grids are applied for the compressed square annulus. Thus the computational accuracy of the compressed square annulus will be decreased. However, we can obtain high computational accuracy by controlling a low reduction ratio of the square annulus.

Both stretched transformed region and compressed transformed region have specific anisotropic permittivity and permeability. The transformed anisotropic Maxwell's equations can be obtained by coordinate transformation. We assume that coordinate system (x, y, z) refers to the original space and coordinate (x', y', z') represents the transformed space. Through coordinate transformation, Maxwell's equations remain form-invariant. The transformation relations between electric/magnetic field $\tilde{E}$ / $\tilde{H}$ in transformed space and E / H in original space are as follows.

$$\tilde{E} = \Lambda^T E \tag{2a}$$
$$\tilde{H} = \Lambda^T H \tag{2b}$$

The permittivity tensor $\tilde{\varepsilon}$ and permeability tensor $\tilde{\mu}$ in the transformed coordinate system are related to the original permittivity ε and permeability μ by the relationships

$$\tilde{\varepsilon} = |\Lambda|\Lambda^{-1}\varepsilon\Lambda^{-\mathrm{T}} \tag{3a}$$
$$\tilde{\mu} = |\Lambda|\Lambda^{-1}\mu\Lambda^{-\mathrm{T}} \tag{3b}$$

The Jacobian matrix Λ is described by

$$\Lambda = \frac{\partial(x, y, z)}{\partial(x', y', z')} \tag{4}$$

We transform the small square region ($r < R_1(\theta)$) to a larger one ($r' < R_1'(\theta')$) and compress the square annulus ($R_1(\theta) < r < R_2(\theta)$) to a thinner one ($R_1'(\theta') < r < R_2'(\theta')$), by using the following transformation functions

$$r(r', \theta') = \begin{cases} \dfrac{R_1(\theta)}{R_1'(\theta')} r', & \text{if } r' < R_1'(\theta') \\ \dfrac{R_2(\theta) - R_1(\theta)}{R_2(\theta) - R_1'(\theta)} \left(r' - R_1'(\theta)\right) + R_1(\theta), & \text{if } R_1'(\theta') < r' < R_2'(\theta') \\ r', & \text{otherwise} \end{cases} \tag{5}$$

There are three steps for transforming from the coordinate (x, y, z) to the coordinate (x', y', z'):

1. Transform from (x, y, z) to cylindrical coordinate (r, θ, z) by the Jacobian matrix Λ_1

$$\Lambda_1 = \frac{\partial (x, y, z)}{\partial (r, \theta, z)} = \begin{pmatrix} \cos\theta & -r\sin\theta & 0 \\ \sin\theta & r\cos\theta & 0 \\ 0 & 0 & 1 \end{pmatrix} \tag{6}$$

2. Transform from (r, θ, z) in original space to (r', θ', z') in transformed space by the Jacobian matrix Λ_2

$$\Lambda_2 = \frac{\partial (r, \theta, z)}{\partial (r', \theta', z')} = \begin{pmatrix} \frac{\partial r}{\partial r'} & \frac{\partial r}{\partial \theta'} & 0 \\ 0 & \frac{\partial \theta}{\partial \theta'} & 0 \\ 0 & 0 & \frac{\partial z}{\partial z'} \end{pmatrix} \tag{7}$$

3. Transform from (r', θ', z') to (x', y', z') by the Jacobian matrix Λ_3.

$$\Lambda_3 = \frac{\partial (r', \theta', z')}{\partial (x', y', z')} = \begin{pmatrix} \cos\theta' & \sin\theta' & 0 \\ -\frac{\sin\theta'}{r'} & \frac{\cos\theta'}{r'} & 0 \\ 0 & 0 & 1 \end{pmatrix} \tag{8}$$

Finally, the Jacobian matrix Λ can be regarded as the product of Λ_1, Λ_2 and Λ_3.

$$\Lambda = \begin{pmatrix} \cos\theta & -r\sin\theta & 0 \\ \sin\theta & r\cos\theta & 0 \\ 0 & 0 & 1 \end{pmatrix} \begin{pmatrix} \frac{\partial r}{\partial r'} & \frac{\partial r}{\partial \theta'} & 0 \\ 0 & \frac{\partial \theta}{\partial \theta'} & 0 \\ 0 & 0 & \frac{\partial z}{\partial z'} \end{pmatrix} \times \begin{pmatrix} \cos\theta' & \sin\theta' & 0 \\ -\frac{\sin\theta'}{r'} & \frac{\cos\theta'}{r'} & 0 \\ 0 & 0 & 1 \end{pmatrix} \tag{9}$$

B. THE STABLE ANISOTROPIC FDTD ALGORITHM

Once the Jacobian matrix Λ is solved, we can obtain anisotropic $\tilde{\varepsilon}$ and $\tilde{\mu}$ in transformed space. For the TM mode, the standard FDTD discretization of anisotropic Maxwell's equations is as follows:

$$D_{z(i,j)}^{n+1} = D_{z(i,j)}^{n} + \Delta t \cdot \left(\frac{H_{y(i+1/2,j)}^{n+1/2} - H_{y(i-1/2,j)}^{n+1/2}}{\Delta x} - \frac{H_{x(i,j+1/2)}^{n+1/2} - H_{x(i,j-1/2)}^{n+1/2}}{\Delta y} \right) \tag{10a}$$

$$E_{z(i,j)}^{n+1} = \xi_{zz} D_{z(i,j)}^{n+1} \tag{10b}$$

$$B_{x(i,j+1/2)}^{n+1/2} = B_{x(i,j+1/2)}^{n-1/2} + \frac{\Delta t}{\Delta y} \cdot \left(E_{z(i,j+1)}^{n+1} - E_{z(i,j)}^{n+1} \right) \tag{11a}$$

$$B_{y(i+1/2,j)}^{n+1/2} = B_{y(i+1/2,j)}^{n-1/2} - \frac{\Delta t}{\Delta x} \cdot \left(E_{z(i+1,j)}^{n+1} - E_{z(i,j)}^{n+1} \right) \tag{11b}$$

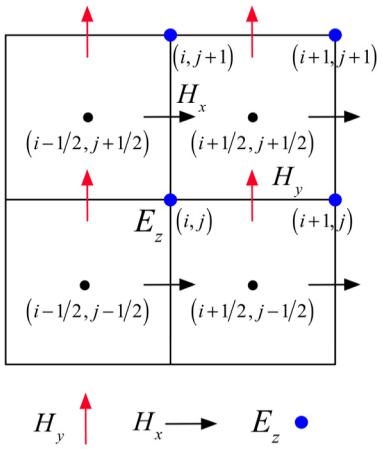

FIGURE 2. The locations of field components in the yee cell.

$$\begin{pmatrix} H_x^{n+1/2} \\ H_y^{n+1/2} \end{pmatrix} = \begin{pmatrix} \zeta_{xx} & \zeta_{xy} \\ \zeta_{yx} & \zeta_{yy} \end{pmatrix} \begin{pmatrix} B_x^{n+1/2} \\ B_y^{n+1/2} \end{pmatrix} \tag{11c}$$

where ξ_{zz} is the reciprocal of the permittivity $\tilde{\varepsilon}_{zz}$, and ζ is the inverse of the 2×2 permeability tensor $\tilde{\mu}$.

The locations of field components in the Yee cell is illustrated in Fig. 2. The ξ and ζ are located at the center of the cell. We develop a stable anisotropic FDTD algorithm for solving the transformed anisotropic Maxwell's equations. To maintain computational stability, E_z, ξ_{zz} and D_z should be evaluated at the same position by the arithmetic average. We first resolve D_z by (10a). Then we solve E_z by the following formula

$$E_{z(i,j)}^{n+1} = \frac{1}{4}\left[\xi_{zz(i-1/2,j+1/2)} + \xi_{zz(i+1/2,j+1/2)} + \xi_{zz(i+1/2,j-1/2)} + \xi_{zz(i-1/2,j-1/2)}\right] D_{z(i,j)}^{n+1} \tag{12}$$

Subsequently, we solve B_x and B_y by (11a) and (11b). Then, applying the similar averaging algorithm mentioned above, we can solve H_x and H_y by

$$H_{x(i,j+1/2)}^{n+1/2} = \frac{1}{2} \cdot \left(\zeta_{xx(i+1/2,j+1/2)} + \zeta_{xx(i-1/2,j+1/2)}\right) B_{x(i,j+1/2)}^{n+1/2} + \frac{1}{4} \cdot \left[\begin{array}{l} \zeta_{xy(i+1/2,j+1/2)} \left(B_{y(i+1/2,j)}^{n+1/2} + B_{y(i+1/2,j+1)}^{n+1/2}\right) \\ + \zeta_{xy(i-1/2,j+1/2)} \left(B_{y(i-1/2,j)}^{n+1/2} + B_{y(i-1/2,j+1)}^{n+1/2}\right) \end{array} \right] \tag{13a}$$

$$H_{y(i+1/2,j)}^{n+1/2} = \frac{1}{2} \cdot \left(\zeta_{yy(i+1/2,j+1/2)} + \zeta_{yy(i+1/2,j-1/2)}\right) B_{y(i+1/2,j)}^{n+1/2} + \frac{1}{4} \cdot \left[\begin{array}{l} \zeta_{yx(i+1/2,j+1/2)} \left(B_{x(i,j+1/2)}^{n+1/2} + B_{x(i+1,j+1/2)}^{n+1/2}\right) \\ + \zeta_{yx(i+1/2,j-1/2)} \left(B_{x(i,j-1/2)}^{n+1/2} + B_{x(i+1,j-1/2)}^{n+1/2}\right) \end{array} \right] \tag{13b}$$

After solving the field $\tilde{E}$ and $\tilde{H}$, we can obtain the field E and H in original space by applying an inverse transformation of (2a) and (2b).

III. NUMERICAL RESULTS

The proposed algorithm is suited for the scenario of a small target in a large domain. The whole computational domain is a multi-scale geometry. However, the proposed algorithm is not suitable for a multi-scale target. If a multi-scale target is enlarged by our transformation method, not only the small-scale part of the target is enlarged, but also the large-scale part of the target is enlarged. The computational domain will be increased as a whole so that the efficiency cannot be improved. Thus, numerical experiments of single-slit diffraction and scattering of a small structure are simulated in this section to demonstrate the computational accuracy advantage of our proposed TO-FDTD with Square Transformed Region (TO-FDTD with STR) algorithm over the original TO-FDTD with Circular Transformed Region (TO-FDTD with CTR) algorithm, The uniform FDTD grid size is applied in the whole computational domain, which is truncated by Convolution Perfectly Matched Layer (CPML) boundaries. The Total-Field-Scattered-Field (TF-SF) approach is used to excite a uniform incident plane wave with the wavelength of 800 nanometers (nm). The horizontally polarized incident wave propagates along the positive x-axis. All calculations have been performed on an Intel Core i5 at 2.7-GHz mac OS with 8-GB RAM.

A. SINGLE-SLIT DIFFRACTION

We first consider the problem of single-slit diffraction. The simulated model is illustrated in Fig.3 (a). Two metal strips face each other with 10 nm slit near the tips. The grid size should be fine enough to accurately model the tiny slit by the standard FDTD algorithm. Therefore, we choose the computational grid size of $\Delta = 2$nm. By applying transformation optics, we enlarge the inner square region (40nm×40nm) 10 times and maintain the outer square region (1200nm×1200nm) unchanged. Accordingly, the square annulus between the square (1200nm×1200nm) and the square (40nm×40nm) is shrunk 1.45 times (thickness changed from 580 nm to 400 nm). The 10 nm slit in original space is transformed to a 100 nm one in transformed space. Consequently, the 100 nm slit can be simulated by the TO-FDTD algorithm with coarse grid size of $\Delta = 20$nm. We use the results of the standard FDTD with fine grid size of $\Delta = 2$nm as reference to compare the computational accuracy of our TO-FDTD with STR algorithm and the TO-FDTD with CTR algorithm.

Figs.3 (b), (d) and (f) show the distributions of electric fields E_z near the slit solved by the standard FDTD algorithm, the TO-FDTD with CTR algorithm and the TO-FDTD with STR algorithm, respectively. It can be seen that the total fields (including incident fields and scattering fields of metal strips) is within the left region of the slit and diffraction fields

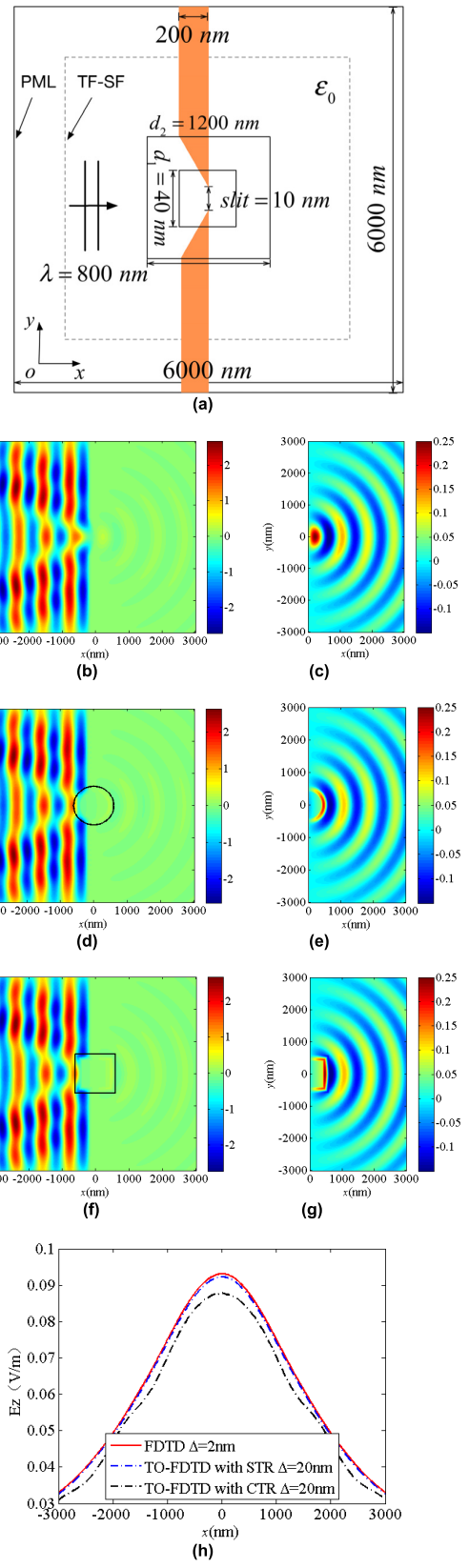

FIGURE 3. Simulation of single-slit diffraction. (a) Structure details. (b) Ez solved by the standard FDTD algorithm with $\Delta = 2$nm. (c) Diffraction fields Ez of Fig.2 (b). (d) Ez solved by theTO-FDTD with CTR algorithm with $\Delta = 20$nm. (e) Diffraction fields Ez of Fig.2 (d). (f) Ez solved by the TO-FDTD with STR algorithm with $\Delta = 20$nm. (g) Diffraction fields Ez of Fig.2 (f). (h) Amplitudes of diffraction fields Ez at $x = 2000$nm.

only exist within the right region of the slit. In Fig.3 (d), the circular region with radius 600 nm is the transformed region for the TO-FDTD with CTR algorithm. As shown in Fig. 3 (f), the square region (1200nm×1200nm) is the transformed region for the TO-FDTD with STR algorithm. The intensity of diffraction fields in Figs.3 (b), (d and (f) are very low since the slit is so narrow that the energy of the incident wave passing through it is very weak. Thus, we display single-slit diffraction fields more clearly, as shown in Figs. 3 (c), (e), and (f) by adjusting the color bar. The waves are bent around the corner of the slit and continue to propagate into the region behind the metal trips rather than propagating along a straight line. It can be seen that the slit diffracts the incident plane wave into a series of circular waves. It can be seen that both electric fields E_z outside of the transformed regions, as shown in Figs. 3 (d-g), are the same as corresponding fields in Figs. 3 (b) and (c), although they are different in the transformed regions.

As for the CPU time, the standard FDTD algorithm requires 126407.6 s to finish the entire simulation and the subgridding FDTD algorithm [8] takes 1842.6 s, while the proposed TO-FDTD with STR algorithm only takes 144.5 s and the TO-FDTD with CTR algorithm needs 144.1 s. A significant speedup is achieved by the TO-FDTD algorithm. Further, we take results of the standard FDTD with fine grid size of $\Delta = 2$nm as reference to compare the computational accuracy of the TO-FDTD with STR algorithm and the TO-FDTD with CTR algorithm. The amplitudes of diffraction fields E_z at $x = 2000$ nm solved by three aforementioned algorithms are plotted in Fig.3 (h). The results of the TO-FDTD with STR algorithm with coarse grid size of $\Delta = 20$ nm agree well with those of the standard FDTD algorithm with fine grid size of $\Delta = 2$nm. However, the results of the TO-FDTD with CTR algorithm with grid size of $\Delta = 20$nm deviates from those of the standard FDTD algorithm with fine grid size of $\Delta = 2$nm. As a result, our TO-FDTD with STR algorithm shows higher computational accuracy than the TO-FDTD with CTR algorithm.

B. SCATTERING OF A SMALL DIELECTRIC SQUARE CYLINDER

In the second example, we simulate scattering of a 2D small dielectric cylinder with the radius of 50 nm and relative permittivity $\varepsilon_r = 12$, which is located at the center of the computational domain, as illustrated in Fig.4 (a). Through transformation optics, we transform the inner square region ($300nm \times 300nm$) to a larger one ($600nm \times 600nm$) and maintain the outer square region (1200nm×1200nm) unchanged. Consequently, the square annulus between the square ($300nm \times 300nm$) and the square (1200nm×1200nm) is compressed 1.5 times (thickness changed from 450 nm to 300 nm). Accordingly, the small cylinder is enlarged twice in transformed space.

Figs.4 (b-d) show the amplitude distribution of electric field E_z near the cylinder resolved by the standard FDTD algorithm with $\Delta = 10$nm, the TO-FDTD with CTR algorithm with $\Delta = 20$nm and the TO-FDTD with STR algorithm with $\Delta = 20$nm, respectively. The total-field domain,

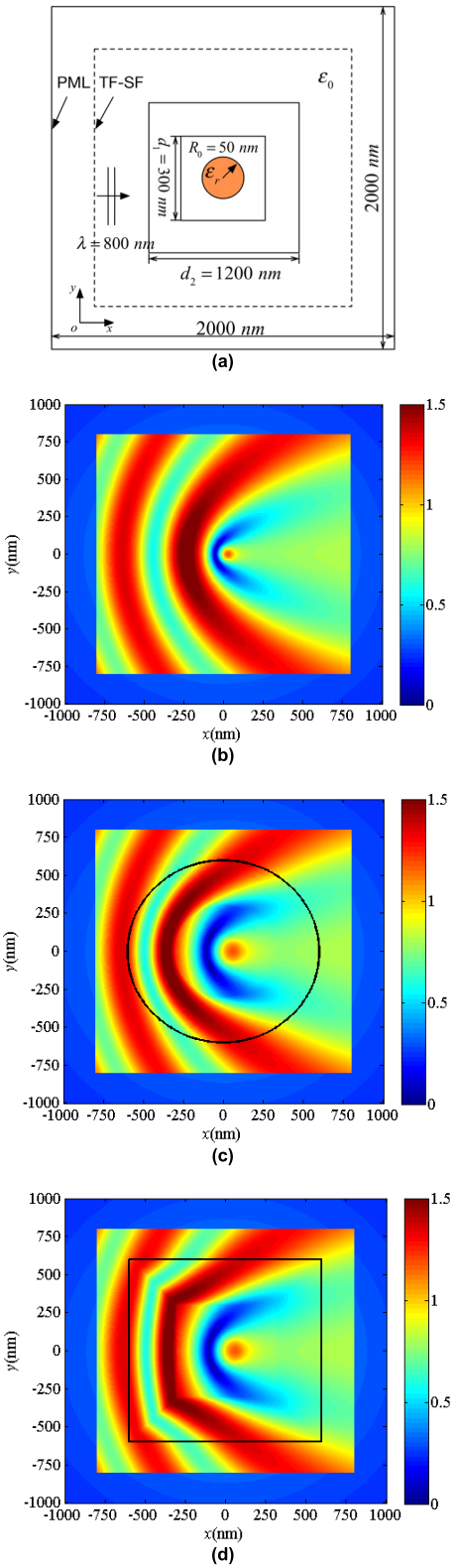

FIGURE 4. Simulation of a 2D cylinder. (a) Structure details. (b) Ez solved by the standard FDTD algorithm with $\Delta = 10$nm. (c) Ez solved by the TO-FDTD with CTR algorithm with $\Delta = 20$nm. (d) Ez solved by the TO-FDTD with STR algorithm with $\Delta = 20$nm.

which includes both incident fields and scattered fields, is confined within the square region ($-800nm < x < 800nm$, $-800nm < y < 800nm$). And the scattered-field domain is outside of the total-field domain, which only contains the scattered fields.

As shown in Fig.4 (c), the circular region ($r < 600nm$) is the transformed region. Fig.4 (d) shows that the square region ($-600nm < x < 600nm$, $-600nm < y < 600nm$) is the transformed region. It can be seen that electric fields E_z outside of the transformed region in Figs.4 (c) and (d) are almost identical to corresponding E_z in Fig.4 (b). Although the coarser grid size of $\Delta = 20$nm is applied in the TO-FDTD with CTR and the TO-FDTD with STR algorithms, they can provide the similar simulation results as the standard FDTD algorithm with the fine grid size of $\Delta = 10$nm. The standard FDTD algorithm takes 60.7 s to finish the entire simulation and the subgridding FDTD algorithm [8] takes 17.1 s, while the proposed TO-FDTD with STR algorithm only requires 9.37 s and the TO-FDTD with CTR algorithm needs 9.22 s.

For further computational accuracy comparison of our TO-FDTD with STR algorithm and the TO-FDTD with CTR algorithm, the amplitudes of scattered fields E_z at $x = -900nm$ are plotted in Fig. 5 (a). As shown in Fig. 5 (a), the results of the TO-FDTD with STR algorithm are more consistent with those of the standard FDTD algorithm than those of the TO-FDTD with CTR algorithm. It demonstrates that our proposed TO-FDTD with STR algorithm has higher computational accuracy.

Then we obtain the bistatic RCS of the small cylinder by the near-to-far field transformation. As shown in Fig. 5 (b), we compare the results solved by these three algorithms, respectively. Good agreement between our proposed TO-FDTD with STR algorithm and the standard FDTD algorithm can be observed even though the grid size of our proposed algorithm is twice that of the standard FDTD algorithm. However, the results of the TO-FDTD with CTR algorithm deviate from those of the standard FDTD algorithm greatly. It also can be seen from the Fig. 5 (b) that the results of our proposed algorithm are well matched with those of the commercial Software Comsol.

Relative errors of the RCS of the small cylinder solved by the TO-FDTD with SRT and the TO-FDTD with CRT are compared in Fig. 5 (c). It can be seen that the TO-FDTD with SRT algorithm proposed in this paper is superior to the TO-FDTD with CRT algorithm in terms of the accuracy.

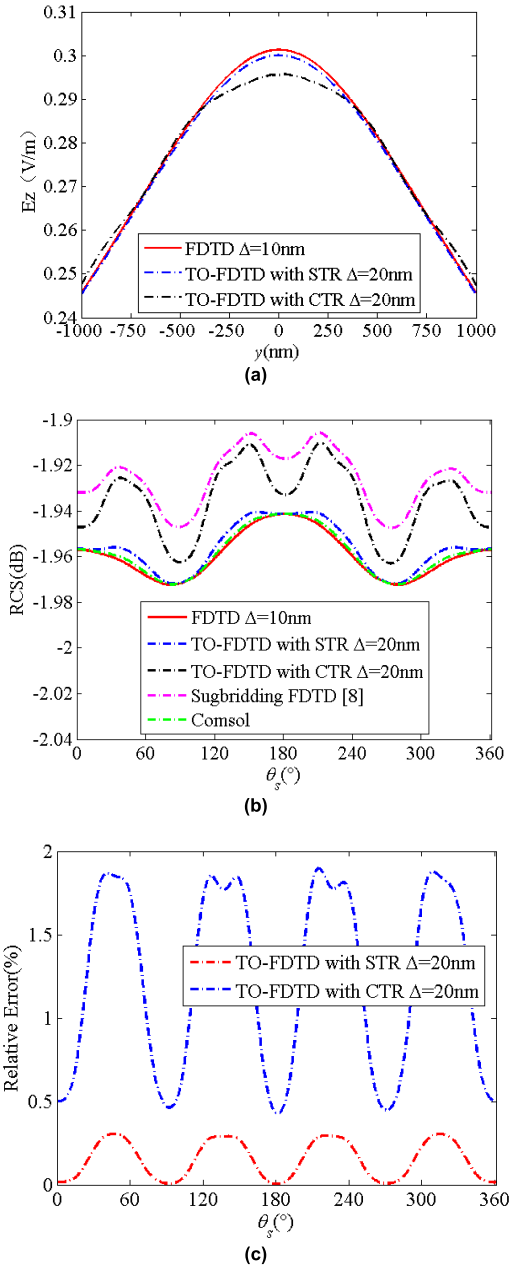

FIGURE 5. (a) Amplitude of scattered electric field Ez at $x = -900nm$. (b) Bistatic RCS versus scattering angle θ_s. (c) Relative errors of RCS solved by the TO-FDTD with SRT and the TO-FDTD with CRT.

C. GPR B-SCAN IMAGE OF BURIED CYLINDERS

To demonstrate one of the applications of the proposed algorithm in ground penetrating radar (GPR). We simulate GPR B-Scan [32] image of targets buried in the sand. Fig. 6 (1) shows that the computational domain is 0.8 m and 0.5 m along the x- and y-direction, respectively. The center of the conducting cylinder with the radius of 0.02 m is located 0.3 m under the surface. The radius of the other conducting cylinder is 0.002 m and its center is located 0.25 m under the surface. The relative permittivity of the sand is $\varepsilon_r = 6$. The transmitting (Tx) antenna and the receiving (Rx) antenna are initially placed at (0.08 m, 0.4 m) and (0.12 m, 0.4 m), respectively. Both the Tx and Rx antennas are considered to be point sources, exciting the current density J_z with the Ricker pulse as follows

$$J_z(t) = -\left(2\pi^2 f^2 \left(t - \frac{\sqrt{2}}{f}\right)^2 - 1\right) e^{-\pi^2 f^2 \left(t - \frac{\sqrt{2}}{f}\right)^2} \quad (14)$$

where $f = 0.9$ GHz.

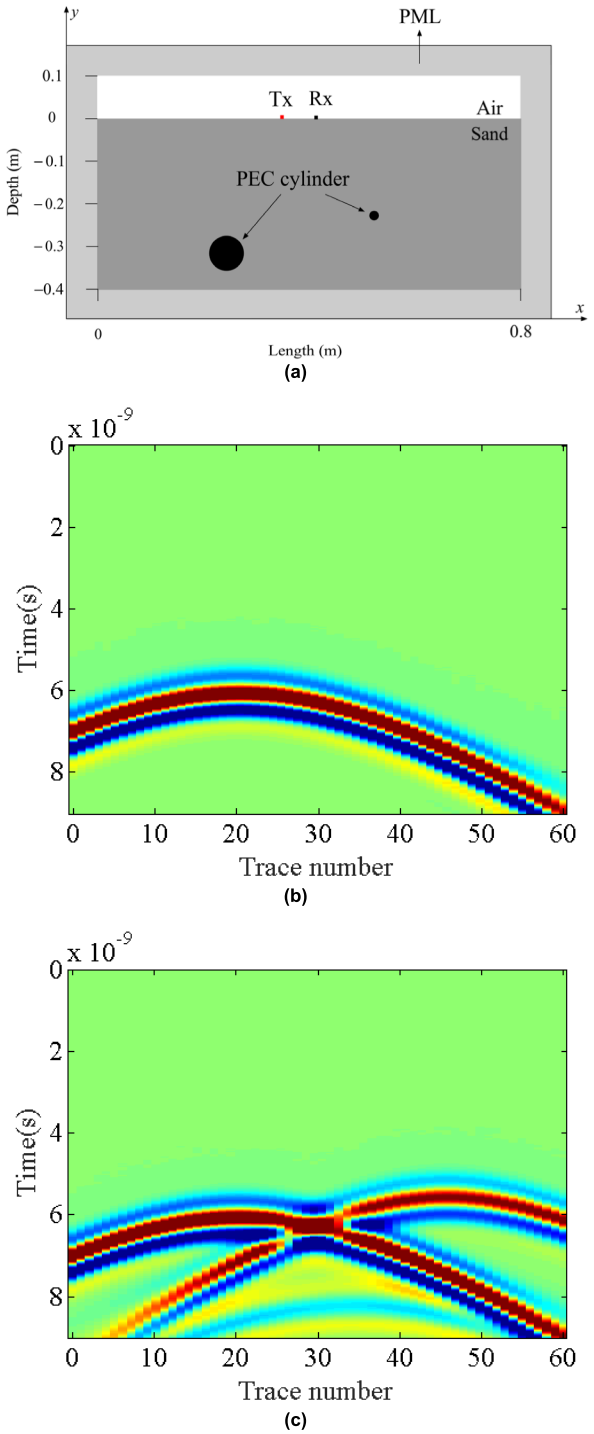

FIGURE 6. GPR B-scan images of buried targets. (a) Structure details. (b) The standard FDTD algorithm with $\Delta = 0.006$ m. (c) The TO-FDTD with STR algorithm with $\Delta = 0.006$ m.

By moving the pair of Tx and Rx antennas along the x-direction with the interval 0.01 m, we can obtain the GPR B-Scan image of the buried targets. The B-scan image, showing the time response of scattering from the buried target, is hyperbolic. For the purpose of comparison, two simulations are run: the standard FDTD with $\Delta = 0.006$ m and the TO-FDTD with STR algorithm with $\Delta = 0.006$ m. The B-scan images by the two algorithms are illustrated in Figs. 6 (2) and (3), respectively.

As shown in Fig. 6 (b), only the scattering response of the big cylinder can be observed, but that of the small cylinder cannot be found. This is because the small cylinder cannot be simulated by the standard FDTD algorithm when its size is less than the grid size. However, as shown in Fig. 6 (c), the responses of both the small and the big cylinder are very clear. The small cylinder can still be simulated by the proposed algorithm, although the used grid size is larger than the size of small cylinder.

IV. CONCLUSION

In this paper, a novel TO-FDTD algorithm is developed for electromagnetic simulation of electrically small structures in a large computational domain. To eliminate staircasing errors caused by curved boundaries of the transformed region, a square transformed region is presented in our TO-FDTD algorithm. The square boundary is parameterized in polar coordinates, so it is easy to be implemented. There are a stretched inner square and a compressed outer square annulus in the transformed region. Through coordinate transformation, a small structure can be enlarged with the stretched inner square. So it can be solved by uniform coarse grids globally, which can improve computational efficiency greatly. However, the stretched region cannot be enlarged arbitrarily. The trade-off is that the compressed square annulus is less solved because of its smaller area. Fortunately, we can adjust the size of the transformed region to obtain acceptable accuracy. In the transformed region, new anisotropic permittivity and permeability are obtained by coordinate transformation. Then, the stable anisotropic FDTD algorithm is developed to solve anisotropic Maxwell's equations in the transformed region. Numerical results show that our proposed TO-FDTD with STR algorithm has higher computational accuracy than the original TO-FDTD algorithm with the same grid size, and has obvious advantages in computational efficiency compared with the standard FDTD algorithm with fine grids. However, the proposed algorithm is only efficient for the multi-scale scenario of an electrically small target in a large computational domain, but not for the multi-scale target. In the future, we will extend the transformation optics based algorithm to solve scattering of a multi-scale target, such as an object with thin coating.

REFERENCES

[1] K. Yee, "Numerical solution of initial boundary value problems involving Maxwell's equations in isotropic media," *IEEE Trans. Antennas Propag.*, vol. AP-14, no. 3, pp. 302–307, May 1966.

[2] L. La Spada, S. Haq, and Y. Hao, "Modeling and design for electromagnetic surface wave devices," *Radio Sci.*, vol. 52, no. 9, pp. 1049–1057, Sep. 2017.

[3] L. Vegni, R. Cicchetti, and P. Capece, "Spectral dyadic Green's function formulation for planar integrated structures," *IEEE Trans. Antennas Propag.*, vol. AP-36, no. 8, pp. 1057–1065, Aug. 1988.

[4] L. La Spada and L. Vegni, "Metamaterial-based wideband electromagnetic wave absorber," *Opt. Express*, vol. 24, no. 6, pp. 5763–5772, 2016.

[5] J. P. Bérenger, "The Huygens subgridding for the numerical solution of the Maxwell equations," *J. Comput. Phys.*, vol. 230, no. 14, pp. 5635–5659, Jun. 2011.

[6] H. AL-Tameemi, J. P. Bérenger, and F. Costen, "Singularity problem with the one-sheet huygens subgridding method," *IEEE Trans. Electromagn. Compat.*, vol. 59, no. 3, pp. 992–995, Jun. 2017.
[7] K. Xiao, D. J. Pommerenke, and J. L. Drewniak, "A three-dimensional FDTD subgridding algorithm with separated temporal and spatial interfaces and related stability analysis," *IEEE Trans. Antennas Propag.*, vol. 55, no. 7, pp. 1981–1990, Jul. 2007.
[8] Z. Ye, C. Liao, X. Xiong, and M. Zhang, "A novel FDTD subgridding method with improved separated temporal and spatial subgridding interfaces," *IEEE Antennas Wireless Propag. Lett.*, vol. 16, pp. 1011–1015, Aug. 2017.
[9] X.-K. Wei, W. Shao, and X.-H. Wang, "Hybrid sub-gridded time-domain method for ground penetrating radar simulations including dispersive materials," *IEEE Access*, vol. 6, no. 1, pp. 15777–15786, Dec. 2018.
[10] X. K. Wei, X. Zhang, N. Diamanti, W. Shao, and C. D. Sarris, "Subgridded FDTD modeling of ground penetrating radar scenarios beyond the Courant stability limit," *IEEE Trans. Geosci. Remote Sens.*, vol. 55, no. 12, pp. 7189–7198, Dec. 2017.
[11] J. Yan and D. Jiao, "An unsymmetric FDTD subgridding algorithm with unconditional stability," *IEEE Trans. Antennas Propag.*, vol. 66, no. 8, pp. 4137–4150, Aug. 2018.
[12] V. Pacheco-Peña, N. Engheta, S. Kuznetsov, A. Gentselev, and M. Beruete, "All-metallic epsilon-near-zero graded-index converging lens at terahertz frequencies," in *Proc. 12th Eur. Conf. Antennas Propag. (EuCAP)*, London, U.K., Apr. 2018, pp. 9–13.
[13] O. Podebrad, M. Clemens, and T. Weiland, "New flexible subgridding scheme for the finite integration technique," *IEEE Trans. Magn.*, vol. 39, no. 3, pp. 1662–1665, May 2003.
[14] N. M. Estakhri, B. Edwards, and N. Engheta, "Inverse-designed metastructures that solve equations," *Science*, vol. 363, no. 6433, pp. 1333–1338, Mar. 2019.
[15] L. La Spada and L. Vegni, "Near-zero-index wires," *Opt. Express*, vol. 25, no. 20, pp. 23699–23708, Oct. 2017.
[16] N. J. Greybush, V. Pacheco-Peña, N. Engheta, C. B. Murray, and C. R. Kagan, "Plasmonic optical and chiroptical response of self-assembled au nanorod equilateral trimers," *ACS Nano*, vol. 13, no. 2, pp. 1617–1624, 2019.
[17] L. La Spada, C. Spooner, S. Haq, and Y. Hao, "Curvilinear metasurfaces for surface wave manipulation," *Sci. Rep.*, vol. 9, no. 1, 2019, Art. no. 3107.
[18] I. Lee, D. Yoo, P. Avouris, T. Low, and S. Oh, "Graphene acoustic plasmon resonator for ultrasensitive infrared spectroscopy," *Nature Nanotechnol.*, vol. 14, pp. 313–319, Feb. 2019.
[19] L. La Spada and L. Vegni, "Electromagnetic nanoparticles for sensing and medical diagnostic applications," *Materials*, vol. 11, no. 4, p. 603, 2018.
[20] L. La Spada, "Metasurfaces for advanced sensing and diagnostics," *Sensors*, vol. 19, no. 2, p. 355, 2019.
[21] V. Pacheco-Peña, M. Beruete, P. Rodríguez-Ulibarri, and N. Engheta, "On the performance of an ENZ-based sensor using transmission line theory and effective medium approach," *New J. Phys.*, vol. 21, no. 4, 2019, Art. no. 043056.
[22] T. M. McManus, L. La Spada, and Y. Hao, "Isotropic and anisotropic surface wave cloaking techniques," *J. Opt.*, vol. 18, no. 4, 2016, Art. no. 044005.
[23] J. Liu, M. Brio, and J. V. Moloney, "Transformation optics based local mesh refinement for solving Maxwell's equations," *J. Comput. Phys.*, vol. 258, pp. 359–370, Feb. 2014.
[24] T. G. Jurgens and A. Taflove, "Three-dimensional contour FDTD modeling of scattering from single and multiple bodies," *IEEE Trans. Antennas Propag.*, vol. 41, no. 12, pp. 1703–1708, Dec. 1993.
[25] S. Dey and R. Mittra, "A locally conformal finite-difference time-domain (FDTD) algorithm for modeling three-dimensional perfectly conducting objects," *IEEE Microw. Guided Wave Lett.*, vol. 7, no. 9, pp. 273–275, Sep. 1997.
[26] I. Zagorodnov, R. Schuhmann, and T. Weiland, "Conformal FDTD-methods to avoid time step reduction with and without cell enlargement," *J. Comput. Phys.*, vol. 225, no. 2, pp. 1493–1507, 2007.
[27] M. R. Cabello, L. D. Angulo, J. Alvarez, A. R. Bretones, G. G. Gutierrez, and S. G. Garcia, "A new efficient and stable 3D conformal FDTD," *IEEE Microw. Wireless Compon. Lett.*, vol. 26, no. 8, pp. 553–555, Aug. 2016.
[28] W. Yu and R. Mittra, "A conformal FDTD algorithm for modeling perfectly conducting objects with curve-shaped surfaces and edges," *Microw. Opt. Technol. Lett.*, vol. 27, no. 2, pp. 136–138, 2000.
[29] T. Xiao and Q. H. Liu, "A 3-D enlarged cell technique (ECT) for the conformal FDTD method," *IEEE Trans. Antennas Propag.*, vol. 56, no. 3, pp. 765–773, Mar. 2008.
[30] G. R. Werner and J. R. Cary, "A stable FDTD algorithm for non-diagonal, anisotropic dielectrics," *J. Comput. Phys.*, vol. 226, no. 1, pp. 1085–1101, Sep. 2007.
[31] G. R. Werner, C. A. Bauer, and J. R. Cary, "A more accurate, stable, FDTD algorithm for electromagnetics in anisotropic dielectrics," *J. Comput. Phys.*, vol. 255, pp. 436–455, Dec. 2013.
[32] Y. Matriche, M. Feliachi, A. Zaoui, and M. Abdellah, "FDTD and improved PSO methods of coupling for identification and localization of buried objects using GPR B-scan response," *Int. J. Remote Sens.*, vol. 35, no. 21, pp. 7499–7518, 2014.

RUONAN CHEN was born in Hebei, China, in 1992. She received the M.S. degree from East China Normal University, Shanghai, China, in 2019. She is currently pursuing the Ph.D. degree with the Macau University of Science and Technology. Her research interests include computational electromagnetics, ground penetrating radar simulations, radar imaging, and planetary science.

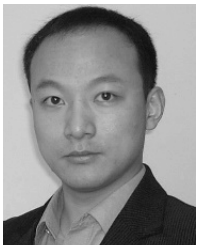

LEI KUANG received the B.S. and M.S. degrees from Anhui University, Hefei, China, in 2001 and 2004, respectively, and the Ph.D. degree from Fudan University, Shanghai, China, in 2008. He was a Visiting Scholar with the Department of Electrical and Computer Engineering, Duke University, NC, USA, from 2016 to 2017, sponsored by the China Scholarship Council. He is currently an Associate Professor with the School of Information Science and Technology, East China Normal University, Shanghai. His current research interests include computational electromagnetics, electromagnetic scattering, and microwave imaging. He received the Excellent Instructor Award for Practical Innovation in East China Normal University, in 2013.

ZHENGQI ZHENG is currently a Professor with the School of Information Science and Technology, East China Normal University, Shanghai, China. His research interests include wireless communication, mobile communication, and radio frequency technology.

QING HUO LIU (S'88–M'89–SM'94–F'05) received the B.S. and M.S. degrees in physics from Xiamen University, Xiamen, China, in 1983 and 1986, respectively, and the Ph.D. degree in electrical engineering from the University of Illinois at Urbana–Champaign, Champaign, IL, USA, in 1989. He was with the Electromagnetics Laboratory, University of Illinois at Urbana–Champaign, as a Research Assistant, from 1986 to 1988, and as a Postdoctoral Research Associate, from 1989 to 1990. He was a Research Scientist and the Program Leader with Schlumberger-Doll Research, Ridgefield, CT, USA, from 1990 to 1995. From 1996 to 1999, he was an Associate Professor with New Mexico State University, Las Cruces, NM, USA. Since 1999, he has been with Duke University, Durham, NC, USA, where he is currently a Professor of electrical and computer engineering. He has authored more than 300 refereed journal articles and 450 conference papers in conference proceedings. His research interests include computational electromagnetics and acoustics, inverse problems, and their applications in geophysics, nanophotonics, and biomedical imaging.